Microporous and Mesoporous Materials 151 (2012) 488–494

Contents lists available at SciVerse ScienceDirect

Microporous and Mesoporous Materials

journal homepage: www.elsevier.com/locate/micromeso

Nanoporous tree-like SiO_2 films fabricated by sol–gel assisted electrostatic spray deposition

Xifei Li [a,b], Abirami Dhanabalan [a], Xiangbo Meng [b], Lin Gu [c], Xueliang Sun [b,1], Chunlei Wang [a,*]

[a] Department of Mechanical and Materials Engineering, Florida International University, 10555 W. Flagler St., Miami, FL 33174, USA
[b] Nanomaterials and Energy Lab, Department of Mechanical and Materials Engineering, University of Western Ontario, London, Ontario, Canada N6A 5B9
[c] Max-Planck Institute for Metals Research, Heisenbergstr. 3, 70569 Stuttgart, Germany

ARTICLE INFO

Article history:
Received 19 March 2011
Received in revised form 1 September 2011
Accepted 1 September 2011
Available online 1 October 2011

Keywords:
Nanoporous
Tree-like
Electrostatic spray deposition
Sol–gel

ABSTRACT

A novel nanoporous tree-like SiO_2 film was synthesized by a sol–gel assisted electrostatic spray deposition (SG-ESD) approach. The sol–gel process employed was better to create SiO_2 with linear cross-link chains for the electrostatic spray deposition. From electron microscopic study, it was found that the as-deposited SiO_2 films possess nanoporous tree-like morphology in macroscale; and monodispersed hollow nanoporous spherical structure in microscale. The formation of the nanoporous "tree" structure is related to the preferential landing of droplets on the substrate and the electrostatic repulsion force among landing droplets during the ESD process. The catalytic effect of hydrochloric acid in the sol–gel system contributes to the formation of the hollow and porous structured SiO_2 spheres. The charge-discharge characteristics of the porous SiO_2 as an anode for Li-ion batteries were briefly evaluated and good long-term cycle performance was reached.

1. Introduction

Porous films show anomalous optical, electronic, thermal, magnetic, and other properties superior to those of their bulk counterparts [1–3]. Of them, porous SiO_2 films have been drawing tremendous research interest in the last two decades because of their wide-range applications, such as microelectronics [4–7], optoelectronic [8–10], multilayer pyroelectric thin-film infrared detectors [11,12], catalysis [13], adsorption [14], sensors [15], membranes [16], template [17], selective separation [18], etc. For instance, porous SiO_2 films have been employed as a super-low dielectric constant material to effectively decrease the interconnection RC signal delay and cross talk in ultra large-scale integrated circuits [6]. Porous SiO_2 films were also shown the refractive index as low as 1.23 and its reflective effect can be controlled by adjusting its porosity [8,12]. Furthermore, it was demonstrated that SiO_2 synthesized by hydrothermal reaction [19], reactive radio frequency sputtering [20], and laser treatment [21] can be employed as anode material for lithium ion batteries [19–21]. Fu et al. reported that the capacity of SiO_2 thin films faded with a slow rate, accounting for about 13.7% after 100 charge/discharge cycles [20]. It is expected that a porous SiO_2 film as a stress-resistant structure with high surface area as an anode can further improve the cycle performance of a lithium ion battery.

Several dry and wet methods have been employed to prepare porous SiO_2 films, including chemical vapor deposition (CVD) [22], electrochemical anodized oxidation [23] and thermal oxidation [24] of a silicon substrate, self-assembled soft templates [25], sol–gel method [26], etc. Of them, CVD method and thermal oxidation are widely used in semiconductor processing because their vapor processes are more suitable for depositing dense SiO_2 thin films of low porosity. Electrochemical anodized oxidation method is the most reported wet electrochemical etching process suitable for the formation of thin porous Si with native SiO_2 film. This method requires a careful selection of several main experimental parameters (such as current, density of illumination, etc.) and special type of Si substrates. Consequently, it remains challenging in order to achieve a precise and repeatable control of the porous structures and dimensions of SnO_2 films. Moreover, the solution-based nature of the electrochemical anodization process limits its application resulting from the intolerable compatibility issues in some device fabrication processes. In comparison, the sol–gel method exhibits many manufacturing advantages such as low cost, high purity, low processing temperature, and good controllability of the chemical composition [27,28]. Hydrolysis of a silicon alkoxide precursor such as tetraethylorthosilicate (TEOS) was previously adopted to prepare the porous SiO_2 films [29]. However, decomposition of the Si based precursor gel alone is usually difficult to precisely control the morphology and porosity of SiO_2 films; besides, mechanical

* Corresponding author. Tel.: +1 305 348 1217; fax: +1 305 348 1932 (C. Wang).
E-mail addresses: xsun@eng.uwo.ca (X. Sun), wangc@fiu.edu (C. Wang).
[1] Tel.: +1 519 661 2111x87759; fax: +1 519 661 3020.

1387-1811/$ - see front matter © 2011 Elsevier Inc. All rights reserved.
doi:10.1016/j.micromeso.2011.09.003

problem such as cracking and peeling are likely to occur during the post annealing process. As Lou et al. reported, the synthetic approaches of hollow structures are divided into four categories: (1) conventional hard templating synthesis, (2) sacrificial templating synthesis, (3) soft templating synthesis, and (4) template-free methods [30]. The template approach is based on the silica formed as the shell on the surfaces of the template particle via the catalyzed hydrolysis and condensation of TEOS. After the silica coating, the template particles are dissolved subsequently to form the hollow structure. However, the disadvantages related to high cost and tedious synthetic procedures have impeded scale-up of the template approach for large scale applications [30].

Regular porous SiO_2 can be synthesized in the aforementioned various approaches, but no research was reported on formation of multi-level hollow and nanoporous SiO_2 with tree-like nanostructure. It is expected that the hollow as well as tree-like nanostructure can be beneficial to increase the effective surface area of SiO_2. Recently we attempted an approach to deposit porous and hollow SiO_2 films with tree-like nanostructure by combining sol–gel method and electrostatic spray deposition (ESD), so-called sol–gel assisted ESD (SG-ESD). The SG-ESD technique provides a simple and versatile method for generating a rich variety of morphologies, such as thin-films, porous and fibrous matrices, and single or multi-component films [31,32]. In this work, we demonstrated that the SG-ESD has many advantages in precise and repeatable fabrication of nanoporous tree-like SiO_2 nanofilms. The sol–gel step produced monodispersed SiO_2 nanoparticles. Moreover unipolar ions induced by the ESD technique charged the sol-solution of low viscosity and thereby helped atomize it into liquid droplets. In addition, the electrical field existing between the nozzle and substrate dominantly determined the trajectories of the droplets and thereby their locations on the substrate.

2. Experimental

2.1. Synthesis of SiO_2 films

A sol–gel method was utilized to prepare the precursor solution: 4.46 mL Tetraethyl orthosilicate (TEOS) and 11.68 mL ethanol (EtOH) were mixed and vigorously stirred using a magnetic stirrer for 10 min. Then a mixture of home-made deionized water (H_2O) and hydrochloric acid (HCl) were added dropwise while stirring to induce the TEOS hydrolysis. The final molar ratio was TEOS:EtOH:H_2O:HCl = 1:10:4:0.05. The solution were then stirred at 40 °C for 5 h and further aged for 24 h at room temperature after the reaction was carried out in a reflux condenser. And then the obtained sol solution (10 mL) was diluted with butyl carbitol (40 mL) to adjust the concentration and the viscosity. The porous SiO_2 films were prepared via a home-made LabView controlled Electrostatic Spray Deposition (ESD) system as shown in Fig. 1. The stainless steel needle (Monoject250, 1.2 mm × 38.1 mm) was connected to a syringe pump using a plastic tube. The precursor solution was delivered by the syringe pump at a flow rate of 2.0 mL h^{-1}. A Direct Current (DC) power supplied with voltage of 4–5 kV between the needle tip and a grounded nickel foam substrate. The high voltage induced a high electrical field between the needle and the substrate, while an ionized area around the tip was produced by the high electrical potential imposed to the needle tip. When the solution was sprayed into the space between the needle tip and the substrate, it split into tiny droplets and deposited on the substrate, both due to the effect of the electrical field. The substrate temperature was controlled at 270 °C by an electric heating module, while the nozzle-to-substrate distance was kept at 3.5–4.0 cm. Both deposition and cooling process took place under ambient atmosphere. The sample under a shadow mask has a round shape with a diameter of 14 mm corresponding to the coin cell diameter, while the effect spray deposition area is much larger with a diameter of 30–40 mm, ensuring the homogeneity of the sample. The as-prepared materials were subsequently annealed at 600 °C for 60 min under argon gas.

2.2. Characterization of porous SiO_2 films

Thermal behavior analysis (thermal gravimetric analysis (TGA) and differential scanning calorimetry (DSC)) was carried out with a Mettler Toledo model TGA/SDTA851e/LF1600 under Argon atmosphere with a heating rate of 10 °C min^{-1} in a temperature range of 25–700 °C. The X-ray diffraction patterns were collected using a D-5000 diffractometer operated at 40 kV and 40 mA, using Cu-Kα radiation (λ = 0.154056 nm) with a scanning rate of 2° min^{-1} between 10° and 90°. Field-emission scanning electron microscopy (FESEM) was performed using a JEOL JSM-6330F SEM operated at 15 kV. High-resolution transmission electron microscopy (HRTEM) was performed using a JEOL 4000EX TEM operated at 400 kV.

2.3. Electrochemical performance of porous SiO_2 films

CR-2032-type coin cells were assembled in a glove box under argon atmosphere, where as-prepared SiO_2 films on nickel foam were used as working electrodes and lithium sheets as counter electrodes and reference electrodes. The electrolyte was 1 M lithium bis (perfluoroethylsulfonyl)imide dissolved in ethylene carbonate:dimethyl carbonate:ethyl methyl carbonate in a 1:1:1 volume ratio. CR-2032-type coin cells were assembled in a glove box under a dry argon atmosphere (moisture and oxygen concentration <1 ppm). Electrochemical impedance spectroscopy measurement was performed using a Versatile Multichannel Potentiostat (VMP3) coupled with a frequency response analyzer. Charge–discharge characteristics were tested galvanostatically between 0.02 and 3.0 V (vs. Li^+/Li) at a current density of 120 mA g^{-1} at room temperature using an NEWARE BTS-610 Battery Test System.

3. Results and discussion

Thermal behavior of SiO_2 gel is presented in Fig. 2a. From the weight loss vs. temperature curve, the apparent weight loss below 200 °C is assigned to the evaporation behavior of ethanol solvent, HCl catalyst, and deionized (DI) water, which also resulted from the desorption of the adsorbed water molecules. In the temperature range from 200 to 600 °C, the residual organic groups, such as hydroxyl and methyl, decomposed and further resulted in mass loss [33,34]. The differential scanning calorimetry (DSC) curve shows that the decomposition occurred at around two endothermic peaks of 295 and 445 °C as well as an exothermic peak of 404 °C. No obvious mass change was observed when the temperature was above 600 °C, implying that the complete decomposition of organic groups completed. According to this thermal behavior, our samples were annealed at 600 °C as a post thermal treatment. Fig. SI-1 in Supporting Information shows the XRD patterns of the SiO_2 films before and after annealing. It is found that the as-deposited SiO_2 is amorphous by nature, no matter before or after an annealing. The crystalline SiO_2 can only be formed above 1600 °C [35].

The morphologies of the as-deposited SiO_2 films were investigated using SEM and TEM. Fig. 3 exhibits the typical SEM and TEM micrographs of SiO_2 films at different magnifications. As shown in Fig. 3a and b, the as-deposited SiO_2 films by the SG-ESD method has unique nanoporous tree-like morphology with self-similarity and organized hierarchical nature. At higher magnification, spherical SiO_2 particles can be found with well-dispersed structures (see Fig. 3c). Furthermore, it is obvious these monodispersed spherical

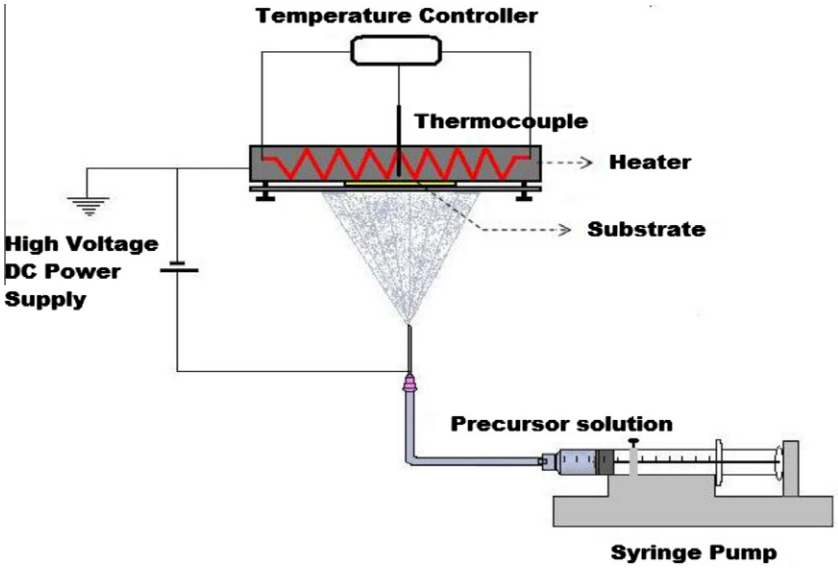

Fig. 1. Schematic diagram of the formation process of nanoporous tree-like SiO_2 films.

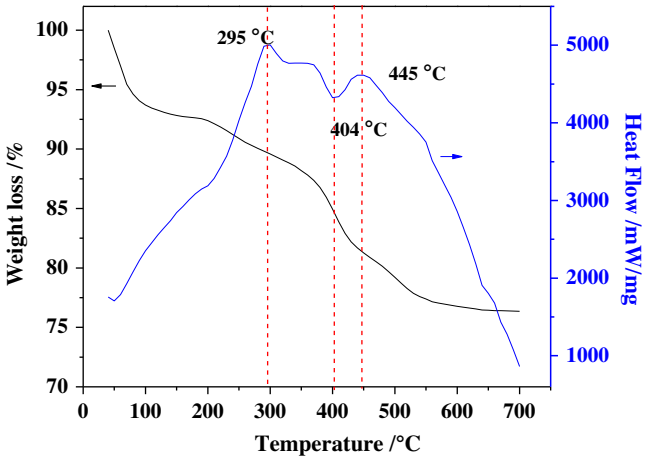

Fig. 2. TGA-DSC curves of SiO_2 gel.

SiO_2 particles with a size of 300–500 nm show hollow porous structure with a pore size of ~7.5 nm. After annealing treatment, the nano-trees structure can still be retained without cracks (Fig. 3e–g). It indicates that the as-deposited SiO_2 films have good thermal stability up to 600 °C, even though the SiO_2 has more different thermal expansion coefficient than nickel, while for the thin film samples cracks can be generated easily after calcination process. The TEM images before and after heat treatment (Fig. 3d and h) corroborate the SEM observation.

In order to confirm the hollow porous structure, the thickness mapping using energy-filtered TEM was performed from the region in Fig. 4a. The image was obtained by dividing a bright-field electron micrograph with the corresponding zero-loss filtered image, the ratio of which is thickness dependent [36]. The micrograph is colorized by the color temperature method (Gatan, Pleasanton, CA, USA) with the legend labeled on the right. In Fig. 4b, the hollow porous structure inside SiO_2 particles, resembling to a cage, was clearly revealed. Nano-tree structure can be also confirmed from cross-sectional SEM observations (see Fig. 4c). Obviously, the height of nano-tree SiO_2, that is, the thickness of SiO_2 films, is ~3 μm. Energy dispersive spectrometer (EDS) was also performed to analyze the SiO_2 films as shown in Supporting Information

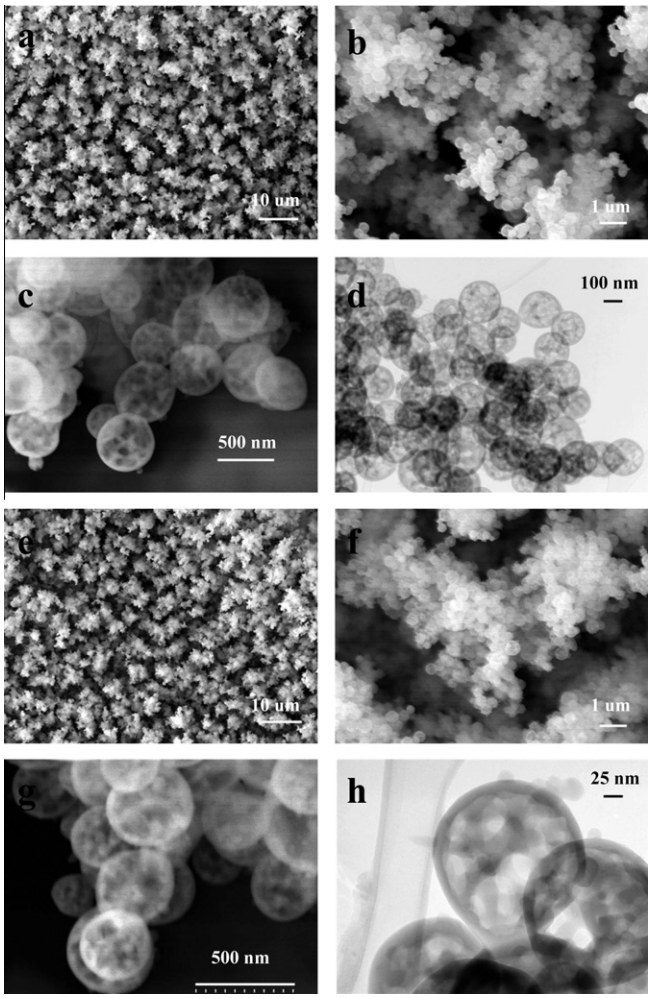

Fig. 3. SEM (a–c and e–g) and TEM (d and h) images of as-deposited samples before calcining (a–d) after calcining (e–h).

(Fig. SI-2). The EDS analysis shows the stoichiometric ratio of C, Si and O of the as-deposited SiO_2 films is 21:14:65. There is no

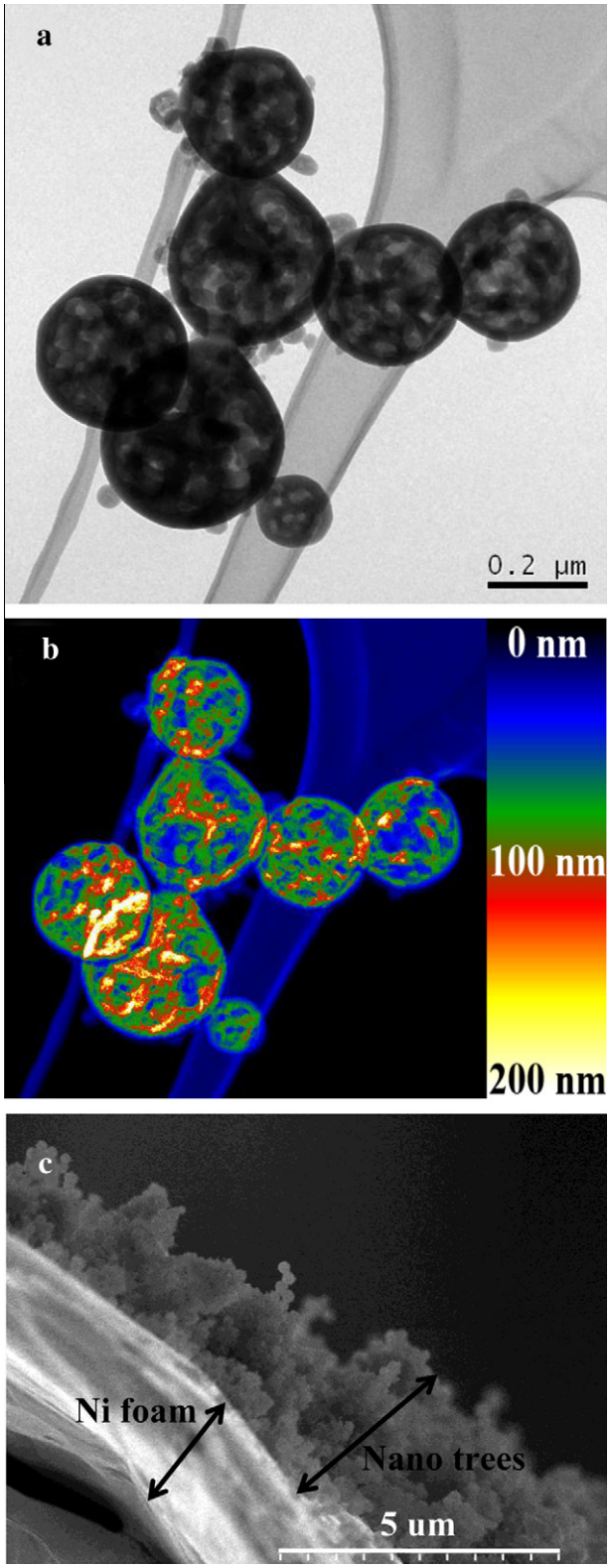

Fig. 4. (a) TEM, (b) thickness mapping of the as-deposited SiO_2 films, and (c) crosssectional SEM images of as-deposited samples after calcining.

carbon existence after calcining SiO_2 films. The stoichiometric ratio of Si and O changed to 31:69. In order to demonstrate that the porosity of SiO_2 films can be tuned by selecting different catalyst for the hydrolysis and condensation of TEOS, we investigated the influence of catalyst on the morphology of SiO_2 films by replacing HCl acid with ammonia. The morphology results show irregular shaped porous structure of the SiO_2 films with a non uniform particle size distribution (see Fig. SI-3). It is reported that both of acid and basic as catalyst show different mechanisms for the hydrolysis and condensation reactions of TEOS. The acid-catalyzed mechanisms are preceded by protonation of $-OCH_2CH_3$ substituent attached to Si, whereas $-OCH_2CH_3$ attacks Si directly for basic catalyst [37]. The reaction kinetics of hydrolysis and condensation are markedly related to the used catalysts. HCl acid catalysis results in the formation of linear structures, whereas under ammonia conditions spherical condensation products are obtained [38]. As a consequence, the different catalysts such as HCl acid and ammonia strongly influence the microstructure and morphology of the resultant SiO_2 films.

During the sol–gel process, H_2O was added into TEOS ethanol solution to induce the TEOS hydrolysis. Hydrochloric acid as the catalyst was added into the solution because the hydrolysis rate of the heterogeneous TEOS-water system is usually low. During the subsequent ESD process, as it is shown in Fig. 5a, the high potential at the nozzle tip induced the surrounding air ionization, resulting in a large amount of positive ions (e.g., O^+, O^{2+}) with high-velocity [39,40]. The ions then charged the diluted sol solution by their bombardment in the surrounding area of the nozzle outlet while they moved towards the substrate. And thereby the sol solution was atomized and dispersed into tiny droplets with the help of electrostatic repulsion force. The resultant droplets moved towards the substrate due to the effect of the electrical field (see Fig. 5b). When the substrate temperature was maintained at 270 °C, there was a temperature gradient between the tip of nozzle and substrate. The maximum saturation charge (Q_{max}) of the droplet is proportional to the square of its radius (r) and can be described by Pauthenier limit [41]:

$$Q_{max} = \frac{12\pi\varepsilon_0 \times \varepsilon_r \times r^2 \times E}{\varepsilon_r + 2} \quad (1)$$

where E is the electric field, ε_0 the permittivity of free space, ε_r the relative permittivity of the droplet. During the flight of droplets towards the substrate, the evaporation of solvents resulted in shrinkage of the droplet with total charge unchanged, which increased the charge density on the surface of droplets. Rayleigh limit can be defined as the point at which coulombic repulsion of the surface charge is equal to the surface tension of the droplets [42], which can be expressed by [31]

$$\frac{Q_R}{m} = \frac{3Q_R}{4\pi \times r^3 \times \rho} = \frac{6}{\rho} \times \left(\frac{\gamma \times \varepsilon_0}{r^3}\right)^{0.5} \quad (2)$$

where Q_R is maximum attainable charge density, m is the mass of the droplet, ρ is the true density of the droplet, and γ is the surface tension of the liquid with respect to the surrounding gas. If the enhanced charge density exceeds the Rayleigh limit, droplets that contain excess positive charge disintegrate into many smaller droplets. It is believed that the coulombic repulsion among smaller droplets prevents them from aggregating into big droplets, which is favorable to the formation of monodispersed nanoscaled SiO_2 particles. When those charged droplets approached the substrate, they would induce imaging charges of the same amount on the substrate. Consequently, the induced imaging force would pull the droplets on the substrate. The non-uniform surface nature of nickel foam substrate caused non-uniform charge density distribution on its surface (Fig. 5c). At the beginning of deposition, some spherical SiO_2 particles were deposited on the special spots (with high charge density) of nickel foam substrate (preferential landing effect) [31]. The subsequent incoming droplets deposited on the initial deposited SiO_2 particles on the substrate under the imaging force. With an evolution of ESD process, several SiO_2 particles developed tree-like

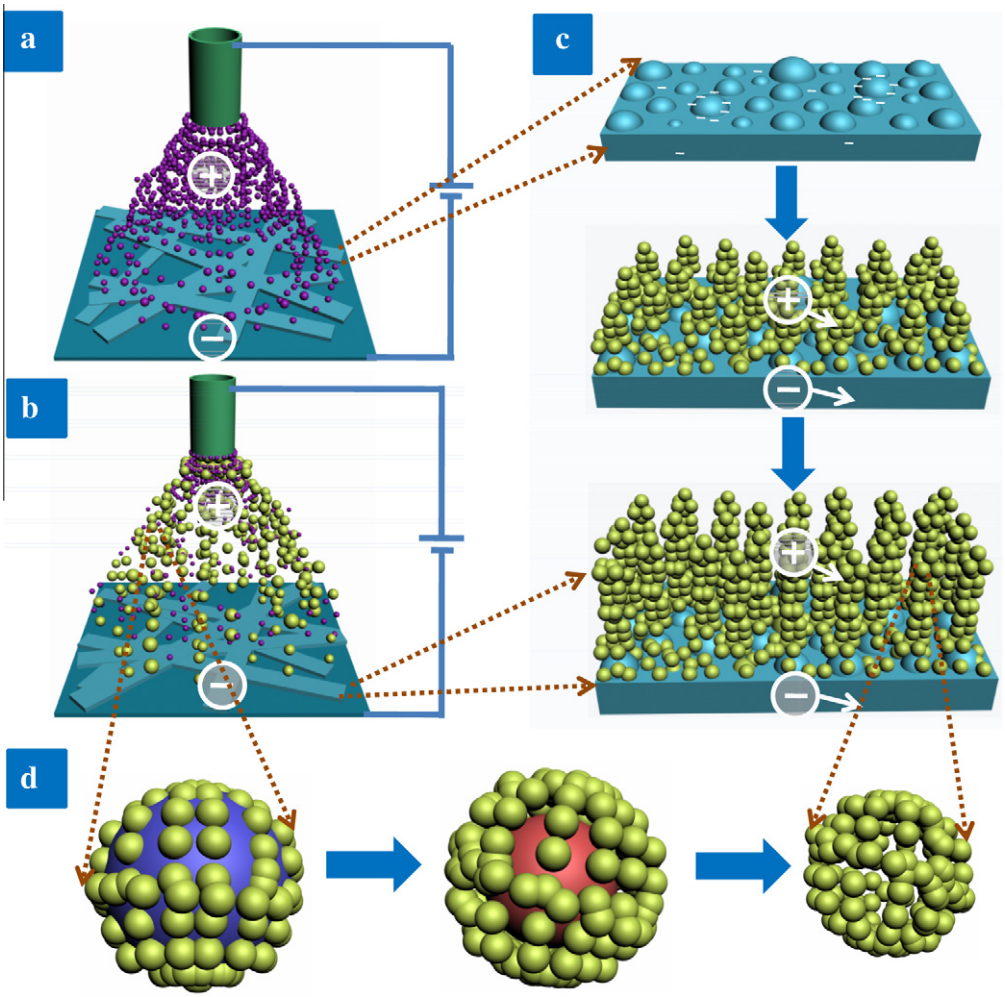

Fig. 5. Schematic mechanism of hollow and nanoporous SiO_2 with tree-like nanostructure on nickel foam synthesized by SG-ESD technique: (a) the high potential at the nozzle tip ionizes the surrounding air and produces a large amount of positive ions; (b) under electrostatic repulsion force the precursor solution was atomized and dispersed into tiny droplets, and the resultant droplets moved towards the substrate; (c) the deposition process of nano-tree-like SiO_2 films was illustrated; and (d) the morphological and structural evolution of nano-porous SiO_2 particles was proposed.

structure (Fig. 5c). Moreover, these "nano-trees" cannot closely contact even aggregate each other due to the electrostatic repulsion force of SiO_2 particles with the same imaging charges. Eventually the nanoporous tree-like SiO_2 films can be constructed.

In case of the catalyst of hydrochloric acid, SiO_2 tended to form linear cross-link chains [43–45]. These molecular chains entangled and easily formed branched structures during the process of ESD [46]. The residual water and hydrochloric acid located among these linear chains and branches. Moreover, ethanol and butyl carbitol filled into the pores among linear chains when the sol solution was diluted due to the needed appropriate viscosity for the ESD process. During the flight of droplets towards the substrate, the change from sol to gel occurred, and spherical SiO_2 particles formed simultaneously. In addition, hydrochloric acid, ethanol, water and butyl carbitol gradually evaporated. As shown in Fig. 5d, the solvents were eliminated from the gel resulting in the hollow porous structure. Due to the fact that the substrate temperature was close to boiling point of butyl carbitol, after the droplets arriving at the substrate, the remaining butyl carbitol solvent inside the particles evaporated simultaneously, which also developed the hollow porous structure. More importantly, the gradual evaporation of hydrochloric acid, ethanol, water and butyl carbitol can effectively avoid the crack even collapse of hollow porous SiO_2 particles.

This unique porous structured SiO_2 should be very interesting for applications where requires large surface areas, such as optoelectronic [7], catalysis [13], sensors [15], and template [17]. We believe this special porous could be beneficial to buffer the huge volume expansion/shrinkage during charge/discharge process as an anode for lithium ion batteries [47,48]. In this research, the electrochemical behavior of the nanoporous tree-like SiO_2 films on nickel foam with a diameter of 14 mm was investigated. The electrochemical impedance spectroscopy (EIS) of SiO_2 films is shown in Fig. 6a at the discharge conditions. The EIS of SiO_2 electrode consists of two depressed semicircles at high and medium frequency domains, respectively, and a line at low frequency region. As depicted by the equivalent circuit in Fig. 6a insert, R_e is the ohmic electrolyte resistance, while R_{sl} corresponds to the resistance for Li^+ migration through the solid electrolyte interface (SEI) film on the surface of SiO_2 and C_{sl} denotes interfacial capacitance corresponding to R_{sl} (corresponding to the first semicircle). And the second semicircle at lower frequency is due to the Li^+ insertion/extraction into SiO_2, that is, the charge transfer at interface between and electrolyte (related with double-layer capacitance (C_{dl}) and charge transfer resistance (R_{ct})). W is the finite-length Warburg impedance that reflects the solid-state diffusion of Li^+ into SiO_2. It can be observed that the simulated impedance spectrum can be well fitted with the experimental one using the equivalent circuit.

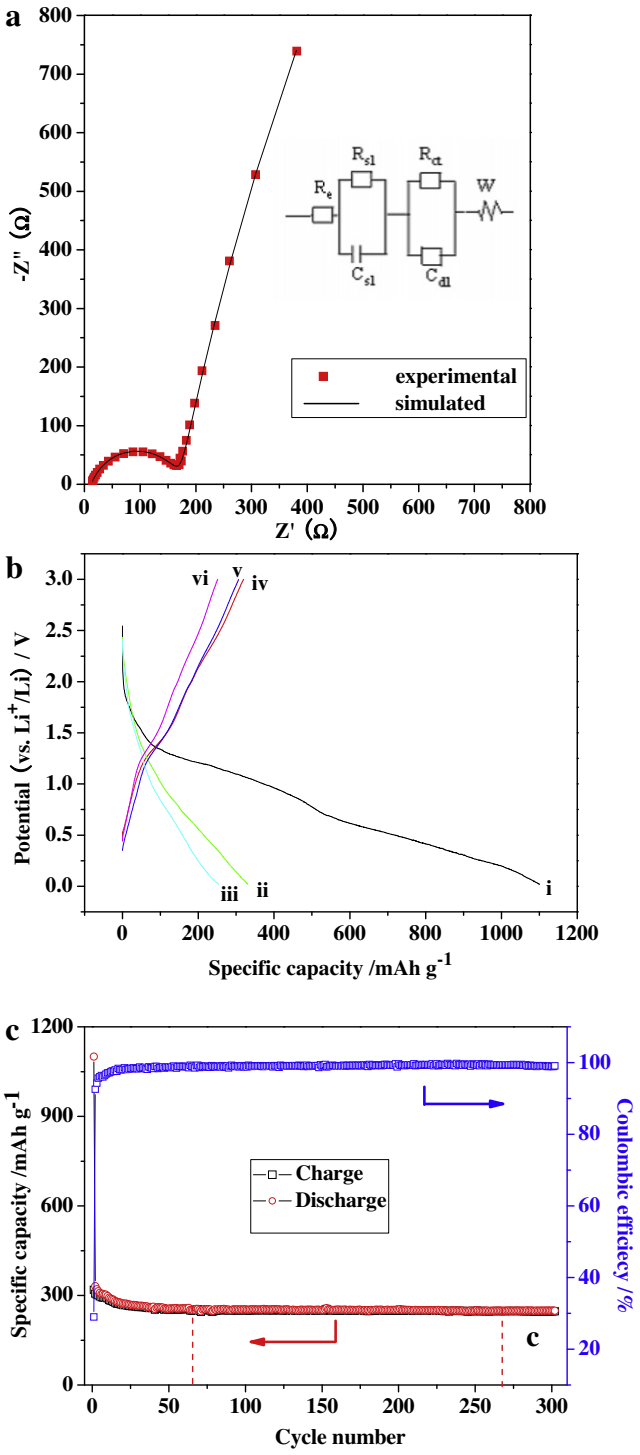

Fig. 6. (a) Electrochemical impedance spectroscopy of the as-deposited SiO_2 films on nickel foam at the discharge conditions; (b) charge/discharge profiles of as-deposited SiO_2 thin films at a current density of 120 mA g^{-1} at a voltage window of 0.02–3.00 V (vs. Li^+/Li): the discharge curves (i) 1st, (ii) 2nd, (iii) 100th, and charge curves (iv) 1st, (v) 2nd, (vi) 100th; (c) reversible charge/discharge capacity and coulombic efficiency verse cycle numbers of the as-deposited SiO_2 films on nickel foam as anode for lithium ion batteries at a current density of 120 mA g^{-1} in a voltage range of 0.02–3.0 V (vs. Li^+/Li) current density of 120 mA g^{-1} in a voltage range of 0.02–3.0 V (vs. Li^+/Li).

Wang et al. proved the electrochemical reduction of nano-SiO_2 and the formation of Li_4SiO_4 and Li_2O as well as Si in the first-discharge, and proposed a possible mechanism of amorphous SiO_2 to store lithium below [19]:

$$SiO_2 + 4Li^+ + 4e^- \rightarrow Li_2O + Si \quad (3)$$

$$2SiO_2 + 4Li^+ + 4e^- \rightarrow Li_4SiO_4 + Si \quad (4)$$

$$Si + xLi^+ + xe^- \leftrightarrow Li_xSi \quad (x \leq 4.4) \quad (5)$$

Another possible mechanism is surface storage as proposed by Jamnik and Maier [49]. It was proposed that excess Li can be accommodated at the interfaces of the nanometer-sized particles [49,50]. So-called Li surface storage can play an important role due to the increased surface area in the nanoporous tree-like structured SiO_2. In our research, SiO_2 films were charged and discharged in a voltage range of 0.02–3.0 V (vs. Li^+/Li) at a current density of 120 mA g^{-1}. The charge/discharge behavior and cycle performance are shown in Fig. 6b and c, respectively. The observed discharge capacity in the first cycle was 1100 mA h g^{-1}, whereas 331 mA h g^{-1} in the second cycle. In the first charge/discharge cycle the large capacity loss is due to the irreversible reactions (reactions (3) and (4)) and gradual SEI film formation on the nanoporous tree-like SiO_2 with high surface area. In the 60th cycle, the discharge and charge capacities of SiO_2 thin films were 256 and 254 mA h g^{-1}, respectively. As it is shown in Fig. 6c, SiO_2 films exhibit obvious capacity fade (22.7% in comparison to that of in the 2nd cycle) in the first 60 cycles (see Fig. 6b inset). However, there is no obvious capacity fade (only 2.3% in comparison to that of in the 60th cycle) from the 60th to the 300th cycle (250 and 247 mA h g^{-1} for the discharge and charge capacities, respectively), indicating excellent reversibility and structural stability of the as-prepared nanoporous tree-like SiO_2. It is believed that the nanoporous tree-like morphology is beneficial for the maximization of contact area between the SiO_2 anode and the electrolyte. Nano walls in the porous structure provide a shortened Li^+ diffusion length. The nanoporous tree-like structure can effectively buffer the volume change during SiO_2 reaction with Li^+. Therefore, our nanoporous tree-like SiO_2 shows better cycle performance than other published data [19–21]. It was recently reported that SiO_2 can be reduced into Si using vaporized Mg [51]. Our research results at this point are very promising considering no conductive additives intentionally included. Future work will be conducted on evaluating porous Si and its composites anodes for lithium ion batteries.

4. Conclusion

In summary, we have successfully synthesized novel nanoporous tree-like SiO_2 films by a sol–gel assisted electrostatic spray deposition approach. The process began with the hydrolysis and condensation of tetraethylorthosilicate via a sol–gel method to form SiO_2 based sol solution. The sol solution was atomized by a high electrostatic field applied in the ESD and the spray was deposited onto a heated substrate. It was confirmed that the SiO_2 films possess porous and nanoporous tree-like morphology in macroscale as well as monodispersed hollow nanoporous spherical structure in microscale. Moreover, the as-deposited SiO_2 films have a good thermal stability up to 600 °C. The SiO_2 films as anodes for lithium ion batteries show no obvious capacity fade from 60th cycle up to the 300th cycle with excellent cycle performance due to the special porous structure.

Acknowledgments

We acknowledge financial support from the US Defense Advanced Research Projects Agency (DARPA) Young Faculty Award Program (Project No. HR0011-08-1-0036), the Air Force Office of Scientific Research (AFOSR FA9550-08-1-0287), American Chemical Society (Petroleum Research Fund, 49301-0N110). We also appreciate the experimental assistant from Mr. Chiwon Kang and support from FIU AMERI facility.

Appendix A. Supplementary data

Supplementary data associated with this article can be found, in the online version, at doi:10.1016/j.micromeso.2011.09.003.

References

[1] M.T. Mark, P.L. Christopher, Science 298 (2002) 1723.
[2] E.D. Mark, Nature 417 (2002) 813–821.
[3] F. Chen, A. Kitai, Thin Solid Films 517 (2008) 622–625.
[4] M. Herrmann, F. Richter, S.E. Schulz, Microelectron. Eng. 85 (2008) 2172–2174.
[5] S.Y. Chang, Y.C. Huang, Microelectron. Eng. 83 (2006) 1940–1949.
[6] A. Link, R. Sooryakumar, R.S. Bandhu, G.A. Antonelli, J. Appl. Phys. 100 (2006) 013507.
[7] N. Kawakami, Y. Fukumoto, T. Kinoshita, K. Suzuki, K. Inoue, Jpn. J. Appl. Phys. 39 (2000) L182–L184.
[8] K. Makita, Y. Akamatsu, A. Takamatsu, S. Yamazaki, Y. Abe, J. Sol–Gel Sci. Technol. 14 (1999) 175–186.
[9] J.Q. Xi, M.F. Schubert, J.K. Kim, E.F. Schubert, M.F. Chen, S.Y. Lin, W. Lin, J.A. Smart, Nat. Photonics 1 (2007) 176–179.
[10] J.Q. Xi, J.K. Kim, E.F. Schubert, Nano Lett. 5 (2005) 1385–1387.
[11] L. Li, L.Y. Zhang, X. Yao, Ceram. Int. 30 (2004) 1843–1846.
[12] X.Q. Wu, X. Yao, M.Q. Wang, L.M. Gao, W. Ren, Integr. Ferroelectr. 51 (2003) 73–79.
[13] X. Bu, P. Feng, G.D. Stucky, Science 278 (1997) 2080–2085.
[14] H.K. Jeong, S. Nair, T. Vogt, L.C. Dickinson, M. Tsapatsis, Nat. Mater. 2 (2002) 53–58.
[15] M.P. Schwartz, S.D. Alvarez, M. Sailor, J. Anal. Chem. 79 (2007) 327–334.
[16] S. Vercauteren, K. Keuzer, E.F. Vansant, J. Luyten, R. Leysen, J. Porous. Mater. 5 (1998) 241–258.
[17] S.H. Lee, P.S. Alegaonkar, U.H. Lee, A.S. Berdinsky, J.B. Yoo, Y.U. Kwon, C.Y. Park, Diamond Relat. Mater. 16 (2007) 326–333.
[18] T. Tsuru, J. Sol–Gel Sci. Technol. 46 (2008) 349–361.
[19] B.K. Guo, J. Shu, Z.X. Wang, H. Yang, L.H. Shi, Y.N. Liu, L.Q. Chen, Electrochem. Commun. 10 (2008) 1876–1878.
[20] Q. Sun, B. Zhang, Z.W. Fu, Appl. Surf. Sci. 254 (2008) 3774–3779.
[21] A.Y. Pidluzhna, I.I. Grygorchak, M.V. Nykypanchuk, B.Y. Venhryn, S.I. Mudry, J. Non-Cryst. Solids 354 (2008) 4433–4436.
[22] A. Barranco, J. Cotrino, F. Yubero, J.P. Espinos, J. Vac. Sci. Technol., A 22 (2004) 1275–1284.
[23] S. Frey, B. Gesillon, F. Ozanam, J.N. Chazalviel, J. Carstensen, H. Foll, R.B. Wehrspohn, Electrochem. Solid-State Lett. 8 (2005) B25–B29.
[24] J.Y. Park, J.H. Lee, Mater. Chem. Phys. 82 (2003) 134–139.
[25] H. Miyata, T. Suzuki, A. Fukuoka, T. Sawada, M. Watanabe, T. Noma, K. Takada, T. Mukaide, K. Kuroda, Nat. Mater. 3 (2004) 651–656.
[26] D. Buso, M. Guglielmi, A. Martucci, G. Mattei, P. Mazzoldi, C. Sada, M.L. Post, Nanotechnol. 17 (2006) 2429–2433.
[27] D.A. Ward, E.I. Ko, Ind. Eng. Chem. Res. 34 (1995) 421–433.
[28] C. Sanchez, B. Lebeau, F. Chaput, J.P. Boilot, Adv. Mater. 15 (2003) 1969–1994.
[29] Y. Liu, H. Chen, L. Zhang, X. Yao, J. Sol–Gel Sci. Technol. 25 (2002) 103–111.
[30] X.W. Lou, L.A. Archer, Z.C. Yang, Adv. Mater. 20 (2008) 3987–4019.
[31] C.H. Chen, E.M. Kelder, J. Schoonman, Thin Solid Films 342 (1999) 35–41.
[32] I.H. Kim, K.B. Kim, Electrochem. Solid-State Lett. 4 (2001) A62–A64.
[33] Z.J. Wu, K. Lee, Y.X. Lin, X.R. Lan, L.Y. Huang, J. Non-Cryst. Solids 320 (2003) 168–176.
[34] N. Suyal, D. Hoebbel, M. Mennig, H. Schmidt, J. Mater. Chem. 9 (1999) 3061–3067.
[35] J.B. Ko, S.W. Lee, D.E. Kim, Y.U. Kim, G. Li, S.G. Lee, T.S. Chang, D. Kim, L.J. Yong, J. Porous. Mater. 13 (2006) 325–330.
[36] L. Gu, Y. Yu, V. Penmatsa, C.L. Wang, J. Maier, P.A.V. Aken, Appl. Phys. Lett. 94 (2009) 231903. 1-3.
[37] C.J. Brinker, J. Non-Cryst. Solids 100 (1988) 31–50.
[38] K. Bredereck, F. Effenberger, M. Tretter, J. Colloid Interf. Sci. 360 (2011) 408–414.
[39] D.S. Chester, United States Patent, No. 3812399, 1974.
[40] I. Panich, T. Nakorn, J. Electrostat. 68 (2010) 254–260.
[41] X.B. Meng, H. Zhang, J.X. Zhu, J. Phys. D Appl. Phys. 41 (2008) 195207.
[42] D.C. Taflin, T.L. Ward, E.J. Davis, Langmuir 5 (1989) 376–384.
[43] I. Strawbridge, A.F. Craievich, P.F. James, J. Non-Cryst. Solids 72 (1985) 139–157.
[44] O.B. Skorodumova, G.D. Semchenko, Y.N. Goncharenko, V.S. Tolstoi, Glass Ceram. 58 (2001) 31–33.
[45] Y.K. Akimov, Instrum. Exp. Tech. 46 (2003) 287–299.
[46] Y. Liu, W. Ren, L.Y. Zhang, X. Yao, Thin Solid Films 353 (1999) 124–128.
[47] J.S. Bridel, T. Azaıs, M. Morcrette, J.M. Tarascon, D. Larcher, Chem. Mater. 22 (2010) 1229–1241.
[48] J.K. Lee, M.C. Kung, L. Trahey, M.N. Missaghi, H.H. Kung, Chem. Mater. 21 (2009) 6–8.
[49] J.Y. Shin, D. Samuelis, J. Maier, Adv. Funct. Mater. 21 (2011) 3464–3472.
[50] H. Lindstrom, S. Sodergren, A. Solbrand, H. Rensmo, J. Hjelm, A. Hagfeldt, S.E. Lindquist, J. Phys. Chem. B 101 (1997) 7717–7722.
[51] Z.H. Bao, M.R. Weatherspoon, S. Shian, Y. Cai, P.D. Graham, S.M. Allan, G. Ahmad, M.B. Dickerson, B.C. Church, Z.T. Kang III, H.W. Abernathy, C.J. Summers, M.L. Liu, K.H. Sandhage, Nature 446 (2007) 172–175.